Microporous and Mesoporous Materials 391 (2025) 113620

Contents lists available at ScienceDirect

Microporous and Mesoporous Materials

journal homepage: www.elsevier.com/locate/micromeso

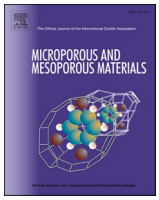

Conjugated microporous polymer containing pyrene and Dibenzo[g,p] chrysene moieties as a luminescent powerhouse for multi-target sensing and environmental safety

Mohamed Gamal Mohamed [a,b,*], Abdul Basit [a], Manivannan Madhu [c], K. Aravinthkumar [c], Awad I. Said [b], Devaraj Manoj [d], Wei-Lung Tseng [c,e,f,**], Shiao-Wei Kuo [a,g,***]

[a] Department of Materials and Optoelectronic Science, Center of Crystal Research, National Sun Yat-Sen University, 804, Kaohsiung, Taiwan
[b] Chemistry Department, Faculty of Science, Assiut University, Assiut, 71515, Egypt
[c] Department of Chemistry, National Sun Yat-sen University, 804, Kaohsiung, Taiwan
[d] Department of Chemistry, Karpagam Academy of Higher Education, Coimbatore, Tamilnadu, 641 021, India
[e] Department of Chemistry and Center for Nanoscience and Nanotechnology, National Sun Yat-sen University, Kaohsiung, 80424, Taiwan
[f] School of Pharmacy, College of Pharmacy, Kaohsiung Medical University, Kaohsiung, 80708, Taiwan
[g] Department of Medicinal and Applied Chemistry, Kaohsiung Medical University, 807, Kaohsiung, Taiwan

ARTICLE INFO

Keywords:
Pyrene
Dibenzo[g,p]chrysene
Conjugated microporous polymer
Chemical sensing
pH sensing
Environmental safety

ABSTRACT

Conjugated microporous polymers (CMPs) have emerged as highly versatile materials, garnering significant attention in recent years due to their unique structural and functional properties. This study presents the development and synthesis of a CMP based on Py-TBNBZ, achieved via a well-established [4 + 4] Schiff base reaction. The reaction involves two primary building blocks: 4,4′,4″,4‴-(pyrene-1,3,6,8-tetrayl)tetrabenzaldehyde (PyBZ-4CHO) and 4,4′,4″,4‴-(dibenzo[g,p]chrysene-2,7,10,15-tetrayl)tetraaniline (TBNBZ-4NH_2). The structural and morphological characteristics of the synthesized Py-TBNBZ CMP material were systematically analyzed using advanced experimental techniques, confirming the successful formation of a robust framework. The Py-TBNBZ CMP prepared in this study showed a BET surface area (S_{BET}) of 497 m^2 g^{-1}. Thermal analysis indicated a decomposition temperature (T_{d10}) of 476 °C and a notable char yield of 74 wt%, as confirmed through BET and TGA measurements. One of the most notable features of the Py-TBNBZ CMP is its strong fluorescence, which enabled its application in chemical sensing. The material exhibited exceptional sensitivity and selectivity, allowing for the detection of K^+ and Fe^{2+} ions and precise pH monitoring over a broad pH range (pH 2–10). The underlying sensing mechanisms were investigated and elucidated. Additionally, the Py-TBNBZ CMP demonstrated remarkable adsorption capabilities for hazardous gas vapors, including ammonia (NH_3) and hydrogen chloride (HCl), underscoring its potential for environmental remediation. The flexibility of the Py-TBNBZ CMP distinguishes it from other CMPs and porous materials, enabling superior performance, enhanced applicability, and improved operational efficiency. This work highlights the advanced capabilities of Py-TBNBZ CMP and contributes to the ongoing development of innovative materials for adsorption, environmental protection, and next-generation sensing technologies.

* Corresponding author. Department of Materials and Optoelectronic Science, Center of Crystal Research, National Sun Yat-Sen University, 804, Kaohsiung, Taiwan.
** Corresponding author. Department of Chemistry, National Sun Yat-sen University, 804, Kaohsiung, Taiwan.
*** Corresponding author. Department of Materials and Optoelectronic Science, Center of Crystal Research, National Sun Yat-Sen University, 804, Kaohsiung, Taiwan.
E-mail addresses: mgamal.eldin34@gmail.com (M.G. Mohamed), tsengwl@mail.nsysu.edu.tw (W.-L. Tseng), kuosw@faculty.nsysu.edu.tw (S.-W. Kuo).

https://doi.org/10.1016/j.micromeso.2025.113620
Received 26 January 2025; Received in revised form 15 March 2025; Accepted 25 March 2025
Available online 25 March 2025

1. Introduction

Porous organic materials (POMs) have garnered significant attention due to their remarkable advancements in preparation methods, functionalization strategies, and the incorporation of diverse functional groups. These materials, often referred to as multifunctional porous materials (MPMs) [1], exhibit a wide range of applications owing to their ability to integrate additional functional components, such as fluorescent moieties, nanoparticles, organic dyes, and fluorophores [2–4]. The development of MPMs addresses the limitations associated with conventional nanomaterials, including organic fluorophores, nanoclusters, and fluorescent nanoparticles, particularly in application-specific contexts [5–7]. Furthermore, POMs demonstrate significant potential in diverse fields such as energy conversion and storage, optoelectronics, catalysis, carbon dioxide capture, and gas separation [8–11]. Their exceptional versatility is attributed to their unique structural and functional properties, enabling flexible and targeted use in these domains [12,13]. This adaptability underscores their value as advanced materials for a broad spectrum of technological and environmental applications. POMs' diverse porosity and functional groups enhance their adaptability, making them valuable for various applications. Their exceptional chemical stability, low density, and unique properties further solidify their importance across multiple fields [14–21].

Various types of porous materials have been developed, each with distinct properties and applications. These include metal-organic frameworks (MOFs) [22], porous organic polymers (POPs) [23], zeolites [24], activated carbons [25], aerogels [26], carbon nanotubes [27], porous glasses [28], metal foams [29], and biologically derived porous materials. CMPs have emerged as promising materials due to advancements in the development of fluorescence-based CMPs and their relatively straightforward synthesis [30–32]. By integrating CMPs with functional moieties, these materials can be tailored for a wide range of applications, including chemical sensing, catalysis, and energy storage in supercapacitors [33–35]. Historically, CMPs have demonstrated effectiveness in detecting various analytes, such as explosives, metal ions, nitro compounds, and organic chemicals, and in biosensing applications [7,36]. However, despite significant progress in the synthesis and application of CMPs, challenges remain in identifying analytes to which these materials exhibit both high sensitivity and selectivity. Enhancing the versatility of CMPs for diverse applications is not only essential but also requires further optimization to maximize their potential across different fields [37–39].

Potassium ions (K^+), as essential intercellular cations, play a critical role in various biological processes, including the regulation of blood pressure and pH levels [40]. Deviations from the normal potassium concentration range of approximately 150 mM can result in serious health conditions, such as diabetes and cardiovascular diseases. Consequently, the early and accurate detection of elevated K^+ levels is vital for reducing the risk of such health complications [30,41,42]. In contrast, the estimation of environmental pH often presents challenges due to the limited linear detection ranges of many organic sensing devices. Nonetheless, pH monitoring is critically important across numerous fields, including food safety, water treatment, environmental research, agriculture, and food security [43]. As such, developing efficient tools for precise pH measurement is imperative for advancing these disciplines. Although conventional techniques are often limited to specific pH ranges, numerous studies have successfully employed CMPs for pH monitoring. Furthermore, the detection of Fe^{2+} ions requires significant expertise due to the complexity of identifying these ions with high sensitivity and selectivity [13,44]. To address the need for a multifunctional tool capable of simultaneously detecting pH levels, Fe^{2+} ions, and K^+ ions, POMs emerge as an ideal choice. POMs offer exceptional functionality, versatility, and adaptability, making them highly suitable for a wide range of applications, including advanced sensing technologies.

During the course of this research, a solid-state Py-TBNBZ-based CMP system was initially developed. Subsequently, it was transformed into a fluorescent material by employing various solvent conditions. This transformation from a solid to a luminescent liquid can be primarily attributed to the expanded π-conjugation core and the functional groups appended to the structure [45]. The resulting material exhibited distinct fluorescence, with an emission peak centered at approximately 575 nm. This fluorescent Py-TBNBZ CMP was employed as a probe for the detection of K^+ and Fe^{2+} ions and functioned effectively as a pH sensor over a broad range of pH values (2–10). Notably, leveraging its pH-sensing capabilities, the material demonstrated the ability to continuously detect harmful gases across multiple cycles. When the prepared Py-TBNBZ CMP was applied to a strip of paper, the paper consistently absorbed vapors released by the target molecules. This innovative CMP not only advances research on porous organic materials (POMs) but also paves the way for the development of porous materials suitable for a diverse array of applications.

2. Experimental section

2.1. Materials

4-Aminophenylboronic acid [$BZB(OH)_2NH_2$], 1,4-dioxane (DO), nitromethane (CH_3NO_2), pyrene (Py), ferric chloride ($FeCl_3$), potassium carbonate (K_2CO_3), 4-fomylphenylboronic acid [$BZB(OH)_2CHO$)], nitrobenzene ($PhNO_2$), anhydrous magnesium sulfate ($MgSO_4$), tetrakis (triphenylphosphine)palladium [$Pd(PPh_3)_4$], and bromine solution (Br_2), were ordered from Alfa Aesar and Sigma-Aldrich; respectively. The TPEH-Br_4 monomer was prepared using the method outlined by our previous studies [Scheme S1] with its spectroscopic data provided in Figs. S1, S2, and S3 [46–48]. The procedure for synthesizing PyBZ-4CHO is provided in the Supporting Information.

2.2. Synthesis of TBNBZ-4NH_2

TPEH-Br_4 (1.66 g, 2.56 mmol) was dissolved in DCM (150 mL) under nitrogen, and $FeCl_3$ (7.54 g, 45.2 mmol) in CH_3NO_2 (10 mL) was added via septum. The mixture was refluxed for 4 h, cooled, and quenched with 250 mL of methanol to afford TBN-Br_4 as a white powder. FTIR (KBr, cm^{-1}, Fig. S4): 3077 (C-H due to phenyl units), 1695. ^{1}H NMR (Fig. S5): 7.84, 8.44, 8.77. For the next step, TBN-Br_4 (2 mmol), $BZB(OH)_2NH_2$ (12 mmol), K_2CO_3 (12 mmol), and $Pd(PPh_3)_4$ (0.2 mmol) were dissolved in 100 mL of DO and 50 mL of H_2O in a 50 mL two-neck flask. The solution was refluxed for 72 h at 115 °C with stirring. After cooling, 20 mL of water was added, and the precipitate was filtered and washed with methanol and water. The yellow solid, TBNBZ-4NH_2. FTIR (Fig. S6): 3451 and 3374 cm^{-1} for NH_2, the stretching vibrations of aromatic C-H and C=C bonds at 3029 and 1617 cm^{-1}. ^{1}H NMR (Fig. S7): 9.1, 7.67, 7.48, 6.73, and 5.3 (NH_2) ppm. ^{13}C NMR (Fig. S8): 148.6 to 114.5 ppm.

2.3. Synthesis of Py-TBNBZ CMP

To prepare Py-TBNBZ CMP, PyBZ-4CHO (3 mmol) and TBNBZ-4NH_2 (3 mmol) were placed in a 25 mL Schlenk tube, and 8 mL each of n-butanol and 1,2-dichlorobenzene (DCB) were combined with 1.5 mL of 6 M acetic acid. The mixture was frozen with liquid nitrogen and degassed using three freeze-pump-thaw cycles under a vacuum. It was then heated at 120 °C for 180 h. The resulting precipitate was filtered and thoroughly washed through Soxhlet extraction with methanol, THF, DMF, and acetone; respectively. The final product, a yellow powder, was identified as Py-TBNBZ CMP. The FTIR spectrum (cm^{-1}): 3027, 1698, and 1599 (C=C). Solid-state ^{13}C NMR analysis: 164.8 ppm (C=N) and 127.9–154.3 (aromatic carbon atoms) ppm.

3. Results and discussion

3.1. Preparation and characterization of TBNBZ-4NH$_2$, PyBZ-4CHO and Py-TBNBZ CMP

The Py monomer, known as a fluorescent probe, features a distinctive π-conjugated framework consisting of four closely linked benzene rings arranged in a rhombic configuration, forming a planar unit rich in electrons [49–51]. Dibenzo[g,p]chrysene (TBN) is a planar polycyclic aromatic hydrocarbon exhibiting D2 symmetry. It can be described as a less curved, restricted variant of tetraphenylethylene (TPEH). This unique structure makes it suitable for various applications, including chemical sensors, organic light-emitting diodes, and nanoporous material design [52,53]. This study successfully synthesized two distinct monomers, TBNBZ-4NH$_2$ and PyBZ-4CHO, as illustrated in Fig. 1(a) and (b). The synthesis of TBNBZ-4NH$_2$ began with the reaction of TPEH-Br$_4$ with FeCl$_3$ in a CH$_3$NO$_2$/DCM solution, yielding TBN-Br$_4$. Subsequently, TBN-Br$_4$ was reacted with BZB(OH)$_2$NH$_2$ in the presence of the base K$_2$CO$_3$

and DO, producing TBNBZ-4NH$_2$ as a yellow solid through Pd-catalyzed Suzuki-Miyaura polymerization. Similarly, PyBZ-4CHO was synthesized by reacting the Py unit with Br$_2$ in a PhNO$_2$ solution to form Py-Br$_4$, followed by a reaction with BZB(OH)$_2$CHO in the presence of K$_2$CO$_3$ and DO, resulting in PyBZ-4CHO as a yellow solid. The FT-IR spectra analysis of TBNBZ-4NH$_2$ and PyBZ-4CHO [Fig. S6] reveals characteristic absorption peaks for the NH$_2$ group in the TBNBZ-4NH$_2$ unit at 3451 and 3374 cm^{-1}. Additionally, the stretching vibrations of aromatic C-H and C=C bonds in the TBNBZ-4NH$_2$ structure correspond to signals at 3029 and 1617 cm^{-1}, respectively. The vibrational modes associated with the stretching of aromatic C-H and C=C bonds in the PyBZ-4CHO unit are identified at 3059 and 1602 cm^{-1}, respectively. Additionally, the characteristic absorption peaks of the CHO group in the PyBZ-4CHO monomer are observed at 2814, 2718, and 1699 cm^{-1} [Fig. S6]. Analysis of the ^{1}H NMR spectra of TBNBZ-4NH$_2$ and PyBZ-4CHO [Figs. S7 and S9] revealed distinct signals. For TBNBZ-4NH$_2$, peaks at 9.10, 7.67, 7.48, 6.73, and 5.30 ppm were attributed to aromatic protons and the NH$_2$ group. Similarly, for PyBZ-4CHO, signals centered at 10.2, 8.2, 8.1, 8.0, and 7.9 ppm corresponded to the CHO group and phenyl rings. The carbon resonance signals for TBNBZ-4NH$_2$ were observed in the range of 148.6 to 114.5 ppm [Fig. S8].

The novel luminescent CMP designated as Py-TBNBZ CMP was synthesized through a Schiff-base coupling reaction [4 + 4] between PyBZ-4CHO and TBNBZ-4NH$_2$, as illustrated in Fig. 2. The Py-TBNBZ CMP was synthesized by reacting PyBZ-4CHO with TBNBZ-4NH$_2$ in a 1:1 mixture of n-butanol and DCB at 120 °C for 180 h. The resulting yellow powder of Py-TBNBZ CMP was found to be insoluble in all tested solvents, confirming the successful crosslinking achieved through Schiff-base coupling. The chemical composition of Py-TBNBZ CMP was further characterized using Fourier-transform infrared (FTIR) spectroscopy and solid-state ^{13}C nuclear magnetic resonance (NMR) spectroscopy (solid-state ^{13}C NMR). The FTIR spectrum [Fig. 3(a)] exhibited characteristic stretching vibrations at 3027, 1698, and 1599 cm^{-1}, pertaining to aromatic C–H stretching, terminal CHO and C=C bonds, respectively. Solid-state ^{13}C NMR analysis [Fig. 3(b)] revealed carbon nuclei signal in 164.8

ppm and the range of 127.9–154.3 ppm, indicative of the presence of C=N bonds and aromatic carbon atoms in the Py-TBNBZ CMP, respectively. These findings provide strong evidence for the successful synthesis and structural integrity of Py-TBNBZ CMP. We have evaluated the chemical stability of the resultant Py-TBNBZ CMP material through FTIR measurements in various solvents, including DCM, THF, MeOH, and EtOH. The FTIR results confirm that all characteristic absorption bands, such as aromatic C-H and C=C stretching, remain present in the Py-TBNBZ CMP framework [Fig. S10]. Thermogravimetric analysis (TGA) demonstrates the exceptional thermal stability of the Py-TBNBZ CMP material compared to other reported POPs, with a high carbon residue of 74 wt% and a decomposition temperature (T_{d10}) of 476 °C, as illustrated in Fig. 3(c). X-ray photoelectron spectroscopy (XPS) was utilized to confirm the elemental composition of Py-TBNBZ CMP, specifically the existence of carbon (C) and nitrogen (N) [Fig. 3(d)]. The XPS survey spectrum revealed characteristic signals at 284 eV and 398 eV, corresponding to carbon and nitrogen, respectively.

Carbon peaks were deconvoluted and identified at 284.3 and 285.3 eV, representing C–C, C=C, and C–N, C=N bonds, respectively [Fig. 3 (e)]. Similarly, nitrogen peaks at 398.9 eV and 401.6 eV were attributed to N–C and N=C bonds ([Fig. 3(f)]. The weight percentages of carbon and nitrogen, as calculated from XPS data, were 93.2 % and 6.8 %,

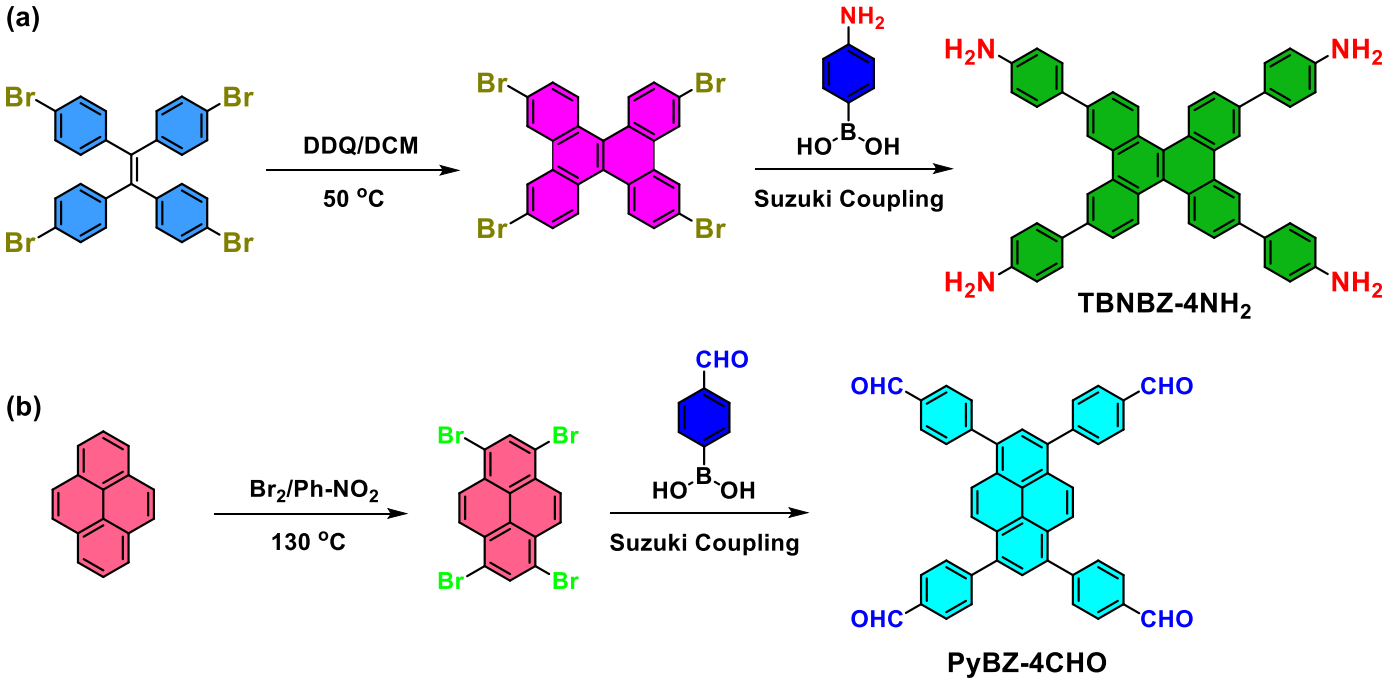

Fig. 1. The preparation of (a) TBNBZ-4NH$_2$ and (b) PyBZ-4CHO from their corresponding TBN-Br$_4$ and Py-Br$_4$.

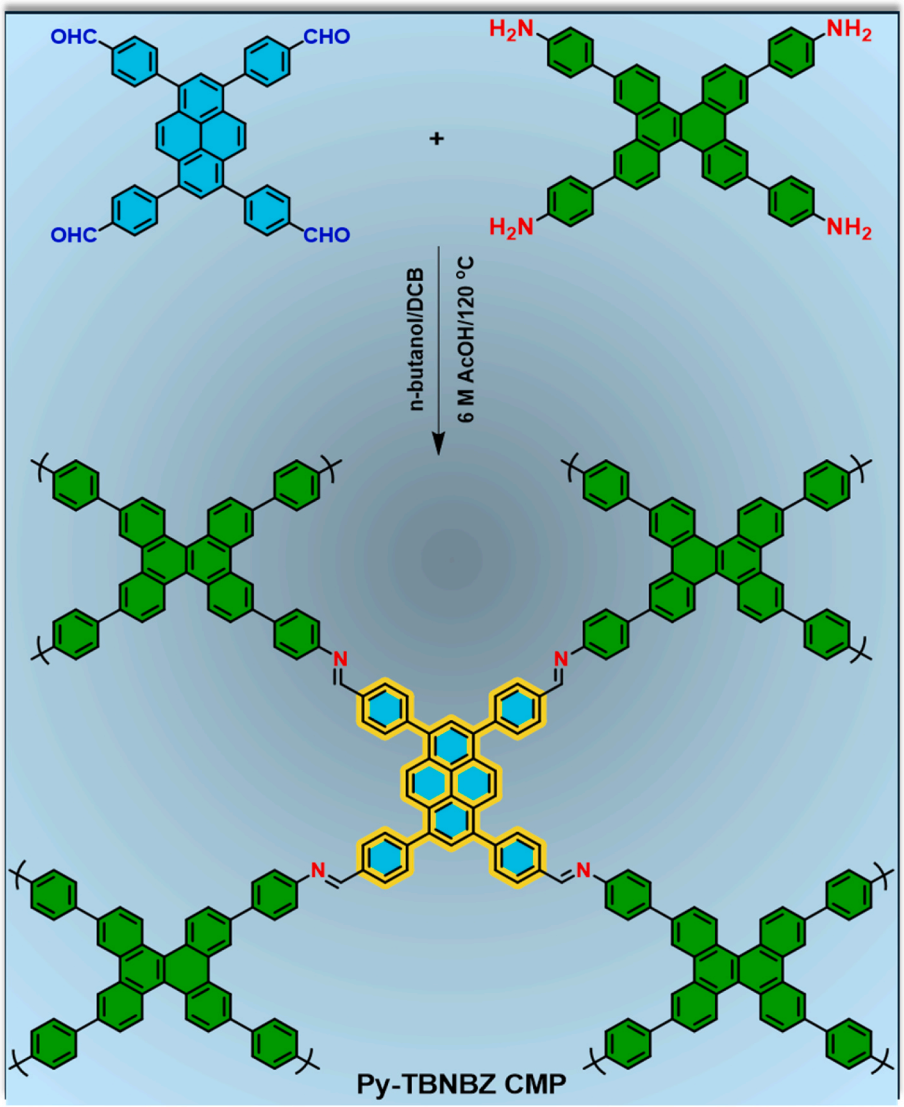

Fig. 2. Scheme representing the synthesis of Py-TBNBZ CMP.

respectively, further validating the composition of Py-TBNBZ CMP. Fig. 4(a) presents the nitrogen adsorption-desorption isotherms for Py-TBNBZ CMP. The material exhibits a specific surface area of 497 m^2 g^{-1}, with type I isotherm behavior characteristic of microporous materials. The pore size distribution, primarily centered around 1.7 nm, confirms the presence of a microporous structure in Py-TBNBZ CMP, as shown in Fig. 4(b). Moreover, the pore volume of Py-TBNBZ CMP is notably high at 0.5 cm^3 g^{-1}, indicating a greater abundance of micropores within the material. Scanning electron microscopy (SEM) images of Py-TBNBZ CMP revealed a non-uniformly agglomerated porous architecture accompanied by a morphology characterized by smaller aggregated nanoparticles [Fig. 4(c) and (d)]. Energy-dispersive spectroscopy (EDS) mapping verified the uniform distribution of carbon (depicted in red) and nitrogen (illustrated in yellow) elements throughout the Py-TBNBZ CMP framework [Fig. 4(e) and (f)]. However, transmission electron microscopy (TEM) analysis showed no evidence of a distinct ordered structure in Py-TBNBZ CMP, as shown in Fig. 4(g) and (h) and Figure S11.

3.2. *Fluorescence properties and metal sensing of Py-TBNBZ CMP*

The photoluminescence (PL) spectra of Py-TBNBZ CMP were analyzed following the preparation of a CMP solution. The preparation process involved sonicating 2 mg of Py-TBNBZ CMP in 2 mL of DMF for 1 h, followed by the collection of the upper solution. This solution exhibited a broad fluorescence emission peak spanning 525–582 nm, with a maximum emission observed at 544.6 nm. As illustrated in Fig. 5 (a), varying excitation wavelengths were employed to examine the corresponding emission peaks. Notably, all subsequent PL measurements consistently exhibited an emission wavelength of 330 nm. The high excitation-independent emission of Py-TBNBZ CMP was attributed to the presence of multiple bonding interactions, including coordination bonds, covalent bonds, and hydrogen bonds. These interactions minimized the intramolecular motion of the functional moieties within the porous framework, thereby enhancing fluorescence emission efficiency [54]. Further investigation was conducted to assess the influence of various solvents—acetone, THF, DCM, ethanol, DMF, and methanol on the PL behavior of Py-TBNBZ CMP. Among these, DMF demonstrated the highest fluorescence intensity [Fig. S12]. This enhanced performance was ascribed to reduced aggregation within the Py-TBNBZ CMP solution and improved exciton mobility, facilitating efficient energy transfer from the CMP network to the Py unit [55]. A stock solution of Py-TBNBZ CMP was prepared by dissolving 5 mg of the material in DMF for subsequent sensing applications, including Fe^{2+} and K^+ ion detection as well as pH monitoring. To evaluate selectivity, a series of anti-interference analytes (10 μM) were prepared. For metal ion sensing,

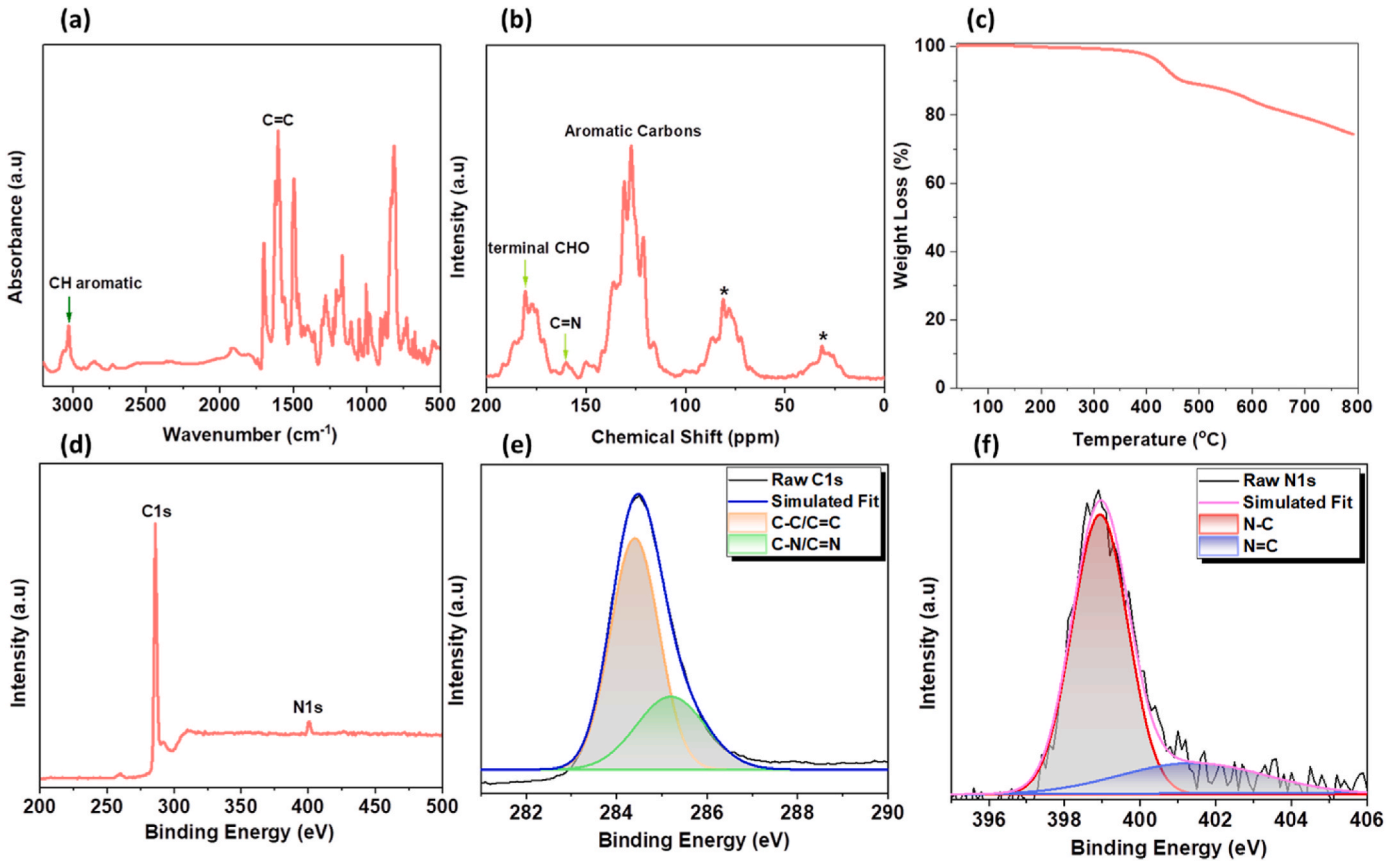

Fig. 3. FT-IR, solid-state ^{13}C NMR, and TGA Analysis of the synthesized Py-TBNBZ CMP. XPS survey analysis of the Py-TBNBZ CMP and XPS fitting data for (e) C1s and (f) N1s.

these analytes included Zn^{2+}, Cr^{3+}, Co^{2+}, Cu^{2+}, Mn^{2+}, Pb^{2+}, and Fe^{3+}, as shown in Fig. S13(a). For potassium sensing, the analytes included Ca^{2+}, Ba^{2+}, Mg^{2+}, and Na^{+}, as depicted in Fig. S13(b). The sensing protocol involved maintaining a constant concentration of the Py-TBNBZ CMP probe while varying the concentrations of the target analytes. Specifically, analyte concentrations ranged from 0.5 to 25 μM for Fe^{2+} sensing and from 1 to 30 μM for K^{+} sensing.

3.3. Sensing of Fe(II) ion using Py-TBNBZ CMP

A previously reported sensing methodology was employed for the detection of Fe(II) ions [56]. The prepared Py-TBNBZ CMP solution, with a total volume of 1.8 mL, was mixed with 0.2 mL of Fe(II) solutions at varying concentrations ranging from 0 to 25 μM. A concentration of 0 μM served as the blank, indicating the absence of Fe(II) ions. As the Fe (II) concentration in the solution increased, the fluorescence intensity of Py-TBNBZ CMP, excited at 330 nm in DMF, exhibited a progressive reduction. Complete quenching of fluorescence at 516 nm was observed at a Fe(II) concentration of 25 μM, as depicted in Fig. 5(b). The quenching behavior was quantified using a linear calibration curve, demonstrating a strong linear relationship between Fe(II) concentrations (8–18 μM) and the fluorescence quenching ratio, expressed as $I\text{-}I_0/I_0$ (Fig. 5(b), inset). Here, I represent the fluorescence intensity of Py-TBNBZ CMP at 516 nm in the absence of Fe(II), while I_0 denotes the fluorescence intensity at varying Fe(II) concentrations. The limit of detection (LOD) for Fe^{2+} ions, determined at a signal-to-noise ratio of 3, was calculated to be 0.5 μM based on the calibration curve. The selective sensing capability of Fe^{2+} by the Py-TBNBZ CMP is primarily attributed to the high binding affinity of Fe^{2+} to the chelation sites formed by atoms such as oxygen (O) and nitrogen (N), as well as the unique pore structure of the Py-TBNBZ CMP framework. The underlying sensing mechanism was validated by analyzing the emission profiles of Py-TBNBZ CMP in the presence of Fe^{2+} and upon subsequent addition of ethylenediaminetetraacetic acid (EDTA). As shown in Fig. S14(a), the fluorescence quenching caused by Fe^{2+} was reversed following the introduction of EDTA, which chelates Fe^{2+}, thereby releasing it from the CMP structure. Furthermore, the process was demonstrated to be reversible, as illustrated by the repeatability of quenching and recovery in alternating cycles [Fig. S14(b)].

3.4. Sensing of potassium ion using Py-TBNBZ CMP

Optical sensors designed for the detection of K^{+} and other metal ions in solution often utilize size-selective, heteroatom-containing macrocycles, including crown ethers, azacrowns, cryptands, and calixarenes, as binding entities. These binding units are typically covalently linked to chromophores or fluorophores, which undergo measurable changes in absorbance or fluorescence upon interaction with metal ions [57]. In this study, K^{+} sensing was conducted following a similar approach to that used for Fe(II) ion detection. Specifically, 1.8 mL of the Py-TBNBZ CMP solution was mixed with K^{+} solutions of varying concentrations (0–25 μM). A concentration of 0 μM served as the blank, indicating the absence of K^{+} in the Py-TBNBZ CMP solution. Upon the addition of K^{+} ions, the fluorescence intensity of Py-TBNBZ CMP in DMF was progressively reduced, ultimately exhibiting complete quenching at a K^{+} concentration of 25 μM. This quenching behavior is depicted in Fig. 5(c), where fluorescence emission is entirely suppressed at the highest K^{+} concentration tested. A linear calibration curve for fluorescence quenching was generated by plotting $(I-I_0)/I_0$ values of Py-TBNBZ CMP against K^{+} concentrations ranging from 2.0 to 15 μM. The linear calibration curve [Fig. 5(c), insert] facilitated the measurement of K^{+} within the specified range, and as a result, Py-TBNBZ CMP exhibited a limit of

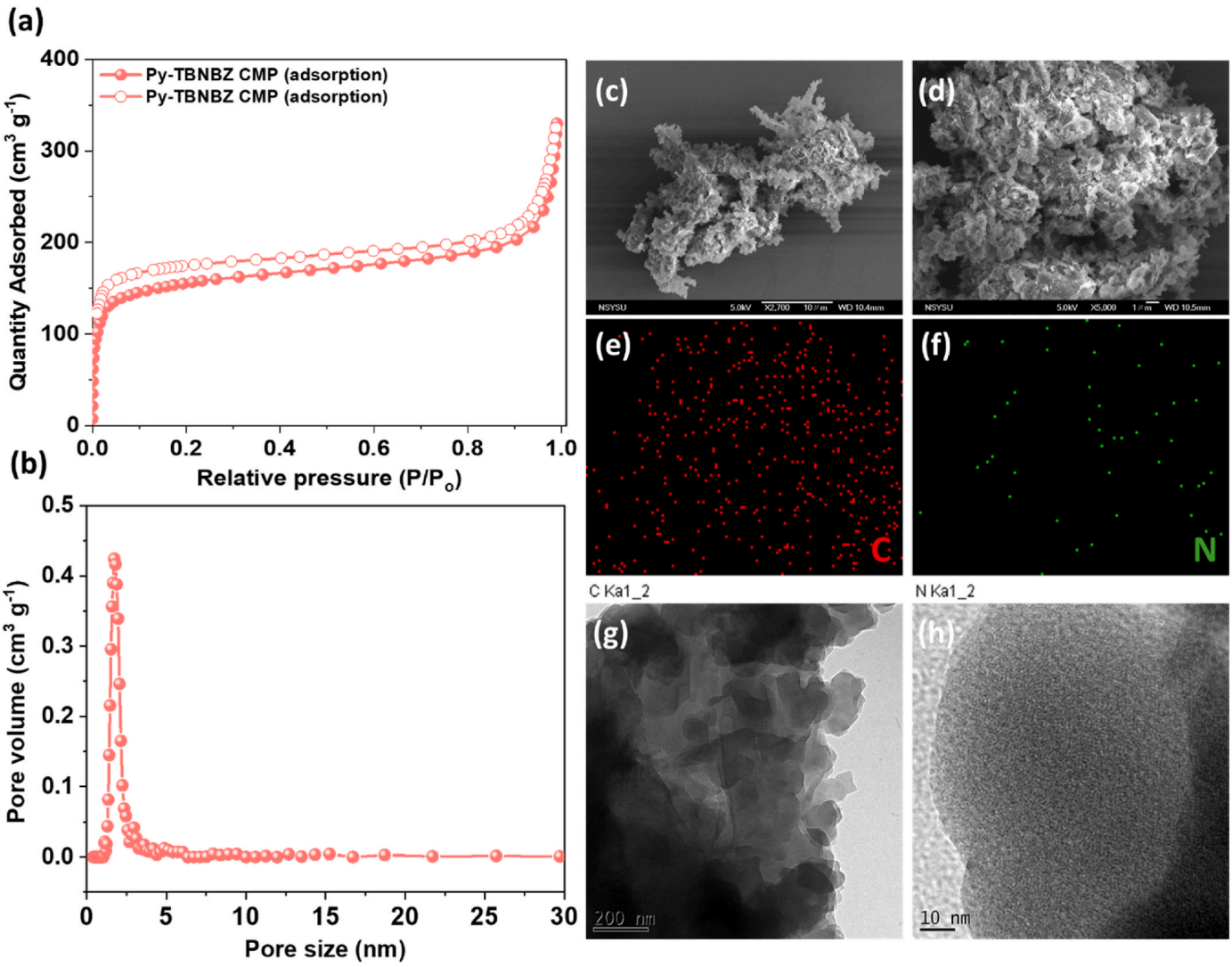

Fig. 4. (a) N_2 adsorption/desorption isotherm, (b) pore size distribution, (c, d) SEM images, (e, f) elemental mapping and (g, h) TEM images recorded for the Py-TBNBZ CMP.

detection (LOD, signal-to-noise ratio of 3) for K^+ ion was 0.08 μM. The observed quenching is induced by cation binding (Fe^{2+} or K^+), which triggers a photoinduced charge transfer (PCT) from the pyrene donor unit to the electron-deficient nitrogen acceptor in the Py-TBNBZ CMP/cation complex [Fig. S15] [58]. Additionally, the insertion of cations between the polymer chains disrupts aggregation, enabling non-radiative intramolecular rotations.

3.5. Effect of pH on Py-TBNBZ CMP probe

In addition to its application in Fe^{2+} and K^+ ion detection, the developed Py-TBNBZ CMP exhibits excellent suitability for pH sensing. The fluorescence emission spectrum of Py-TBNBZ CMP was recorded at various pH values using the maximum excitation and emission wavelengths of 330 nm and 516 nm, respectively, as shown in Fig. 6(d). At these fixed wavelengths, the fluorescence intensity and emission characteristics of Py-TBNBZ CMP were systematically measured across a pH range of 2.0–10.0. As illustrated in Fig. 6(d), the fluorescence intensity of the Py-TBNBZ CMP emission peak at 511 nm gradually decreased with decreasing pH. Notably, the fluorescence intensity recovered steadily as the pH increased from 7.0 to 10.0. At a pH of 10.0, the fluorescence intensity was completely recovered, indicating the sensitivity of Py-TBNBZ CMP to alkaline conditions.

Furthermore, a slight red-shift of the fluorescence peak was observed at the higher pH solution (from 516 to 530 nm). Likely, quenching caused by protonation (low pH) is attributed to PCT from pyrene (donor) to iminium nitrogen (acceptor) [58].

3.6. Paper-based sensor for detection of HCl and ammonia vapor using Py-TBNBZ CMP probe

The detection of hydrogen chloride (HCl) and ammonia (NH_3) vapors is essential for industrial, environmental, and safety purposes. HCl, a toxic and corrosive gas commonly used in chemical manufacturing and metal processing, can cause respiratory harm, equipment corrosion, and environmental damage. Similarly, ammonia, widely employed in agriculture and refrigeration, poses risks to ecosystems and can lead to respiratory issues and other health concerns. The serious risks associated with HCl and NH_3 vapors highlight the urgent need for precise, sensitive, and easy-to-use detection methods to ensure effective monitoring across various environments. The Py-TBNBZ CMP material, when applied to filter paper, demonstrated its utility as a convenient method for detecting HCl and NH_3 vapors. The detection process was performed over five consecutive cycles and relied solely on visual observation, as shown in Fig. 5(e). This approach highlights the potential of Py-TBNBZ CMP as a simple and effective platform for real-time vapor monitoring.

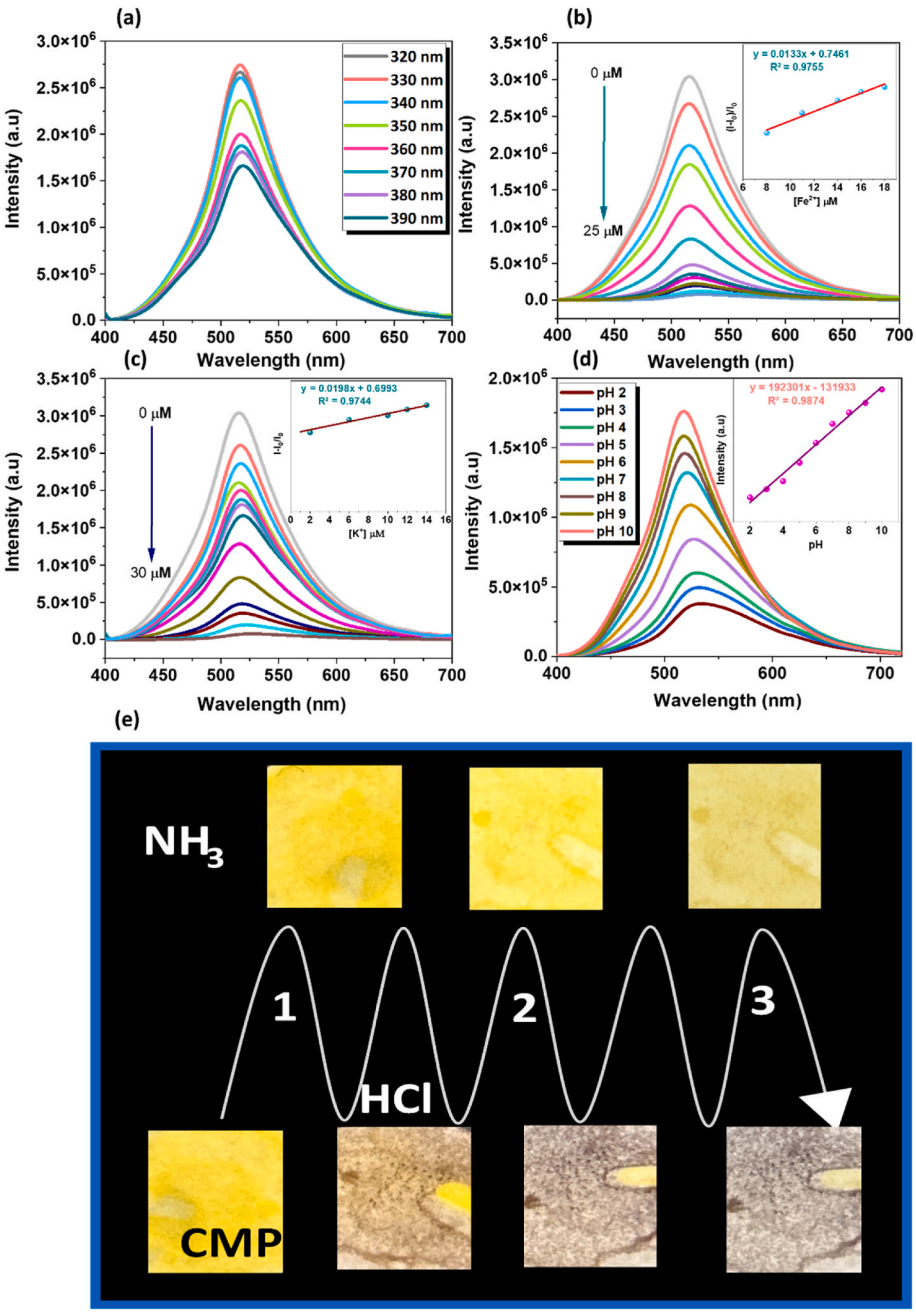

Fig. 5. The fluorescence emission spectrum of the Py-TBNBZ CMP showing excitation independent (a), Sensing of Fe^{2+} ion and their linear calibration curve (insert) (b), Sensing of K^{+} ion and their linear calibration curve (insert) (c), sensing of pH from the range of pH 2.0–10.0 (d) (The excitation wavelength was set to be 330 nm), and visible absorbance of the HCl and ammonia vapor adsorption (e).

However, the HCl vapor absorbed by the Py-TBNBZ CMP shows clear changes. Alternatively, the solution of ammonia shows a clear difference from HCl vapor. These findings show that Py-TBNBZ CMP on filter paper offers a versatile and flexible method for identifying various vapor phases, including HCl and NH_3, using a colorimetric approach. Fig. 6 shows that the Py-TBNBZ CMP demonstrates reversible protonation-deprotonation behavior when exposed to NH_3 and HCl vapor. When the material is exposed to HCl vapor, the acidic environment induces protonation of these nitrogen groups, resulting in a positively charged framework. Conversely, upon exposure to NH_3 vapor, the nitrogen-containing groups in the Py-TBNBZ CMP framework undergo deprotonation, leading to a neutralized state and the Py-TBNBZ CMP retained its original color even after exposure to concentrated NH_3 vapor, a change that was clearly visible to the naked eye [59,60]. Fig. S16 illustrates the electronic distributions of the HOMO and LUMO for both deprotonated and protonated Py-TBNBZ CMP. In both forms, the HOMO is primarily localized on the TBNBZ moiety. The LUMO of the deprotonated Py-TBNBZ CMP is delocalized over the PyBZ moiety, whereas in the protonated Py-TBNBZ CMP, the LUMO is concentrated around the protonated nitrogen and its surrounding conjugated system. This aligns with chemical intuition, as the LUMO represents the region with the highest electron-accepting tendency. The protonated nitrogen, carrying a positive charge, exhibits the strongest electron-accepting ability. The HOMO-LUMO energy gaps for the deprotonated and protonated Py-TBNBZ CMP are 3.24 eV and 2.47 eV, respectively, with the smaller gap in the protonated form indicating greater reactivity.

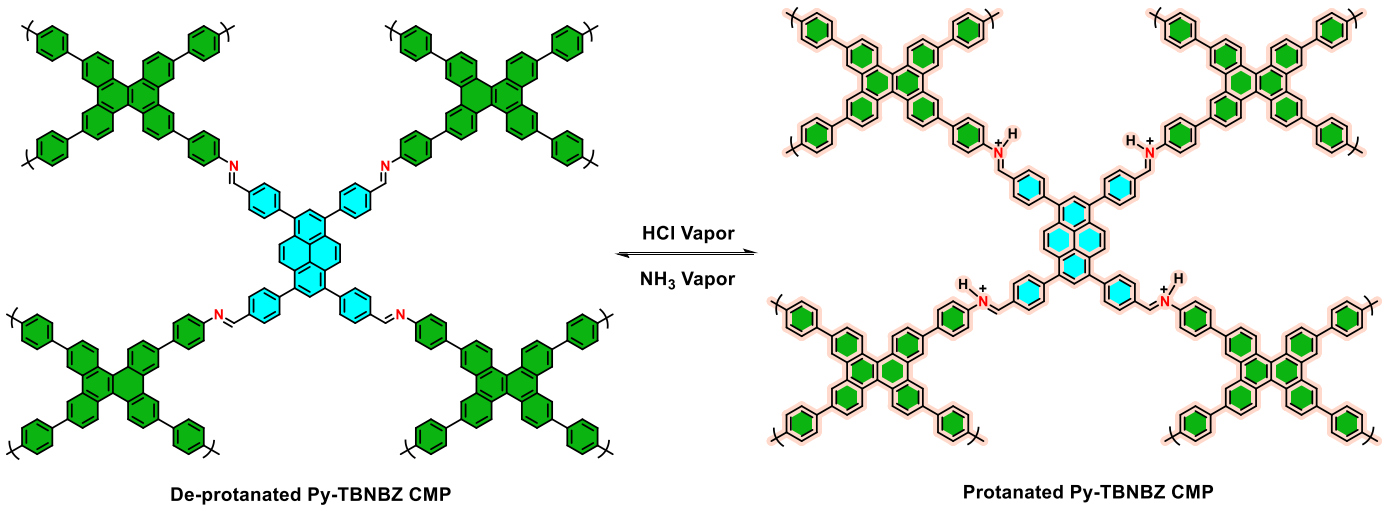

Fig. 6. Schematic scheme for the reversible protonation−deprotonation nature of the Py-TBNBZ CMP in the presence of vapor HCl and NH_3.

4. Conclusions

This study successfully demonstrated the versatility and efficacy of the synthesized Py-TBNBZ CMP across a range of fluorescence-related applications. The Py-TBNBZ CMP probe exhibited exceptional performance in four key areas: (i) detection of Fe^{2+} ions with a minimum detection limit of 0.5 μM within a specified range, (ii) detection of K^+ ions with a comparable minimum detection limit of 0.08 μM, (iii) pH measurement over a broad range from pH 2 to 10, and (iv) monitoring of hazardous gases, including HCl and ammonia, across multiple detection cycles. These findings underscore the adaptability and robustness of Py-TBNBZ CMP as a multifunctional sensing platform. Furthermore, the results encourage continued exploration and development of analogous porous materials to expand their potential applications in sensing, environmental monitoring, and related fields.

CRediT authorship contribution statement

Mohamed Gamal Mohamed: Writing – review & editing, Writing – original draft, Supervision, Methodology, Investigation, Formal analysis, Data curation, Conceptualization. **Abdul Basit:** Data curation, Conceptualization. **Manivannan Madhu:** Formal analysis, Data curation. **K. Aravinthkumar:** Data curation. **Awad I. Said:** Formal analysis. **Devaraj Manoj:** Formal analysis. **Wei-Lung Tseng:** Supervision, Funding acquisition. **Shiao-Wei Kuo:** Supervision, Funding acquisition.

Data availability

Data will be made available on request.

Declaration of competing interest

The authors declare that they have no known competing financial interests or personal relationships that could have appeared to influence the work reported in this paper.

Acknowledgments

This study was supported financially by the National Science and Technology Council, Taiwan, under contracts NSTC 113-2223-E-110-001- and 113-2221-E-110-012-MY3 and the (NSYSUKMU113-P09) for funding this study. We also thank the Center for Nanoscience and Nanotechnology of National Sun Yat-sen University for helping us measure material properties. The authors thank the staff at National Sun Yat-sen University for their assistance with the TEM (ID: EM022600) experiments.

Appendix A. Supplementary data

Supplementary data to this article can be found online at https://doi.org/10.1016/j.micromeso.2025.113620.

Data availability

The data that has been used is confidential.

References

[1] Y.G. Alfaro, P. Aranda, F.M. Fernandes, B. Wicklein, M. Darder, E.R. Hitzky, Multifunctional porous materials through ferrofluids, Adv. Mater. 23 (2011) 5224–5228, https://doi.org/10.1002/adma.201101364.
[2] J. Wu, F. Xu, S. Li, P. Ma, X. Zhang, Q. Liu, R. Fu, D. Wu, Porous polymers as multifunctional material platforms toward task-specific applications, Adv. Mater. 31 (2019) 1802922, https://doi.org/10.1002/adma.201802922.
[3] A.I. Said, M.G. Mohamed, M. Madhu, P.N. Singh, S.V. Chaganti, M.H. Elsayed, W. L. Tseng, F.M. Raymo, S.W. Kuo, Bifunctional luminescent conjugated microporous polymers containing BODIPY and tetraphenylethene units for highly efficient energy storage and enhanced sensing of Cu^{2+} ions, Polymer 300 (2024) 126988, https://doi.org/10.1016/j.polymer.2024.126988.
[4] K. Yuan, L. Jiang, Y. Xing, J. Zhang, J. Zhang, X. Ye, G. Ma, S. Song, C. Liu, Facile synthesis and study of functional porous organic polyaminals with ultrahigh adsorption capacities and fast removal rate for rhodamine B dye, Micropor. Mesopor. Mater. 344 (2022) 112234, https://doi.org/10.1016/j.micromeso.2022.112234.
[5] E. Sivasurya, R. Atchudan, M.G. Mohamed, A. Thangamani, S. Rajendran, A. Jalil, P.K. Kalambate, D. Manoj, S.W. Kuo, Electrocatalytic conversion of CO_2 into selective carbonaceous fuels using metal-organic frameworks: an overview of recent progress and perspectives, Mater. Today Chem. 44 (2025) 102538, https://doi.org/10.1016/j.mtchem.2025.102538.
[6] W.T. Chung, I.M.A. Mekhemer, M.G. Mohamed, A.M. Elewa, A.F.M. EL-Mahdy, H. H. Chou, S.W. Kuo, K.C.W. Wu, Recent advances in metal/covalent organic frameworks based materials: their synthesis, structure design and potential applications for hydrogen production, Coord. Chem. Rev. 83 (2023) 215066, https://doi.org/10.1016/j.ccr.2023.215066.
[7] M.G. Mohamed, H.Y. Hu, S. Santhoshkumar, M. Madhu, T.H. Mansoure, C. W. Hsiao, Y. Ye, C.W. Huang, W.L. Tseng, S.W. Kuo, Design and synthesis of bifunctional conjugated microporous polymers containing tetraphenylethene and bisulfone units for energy storage and fluorescent sensing of p-nitrophenol, Colloids Surf. A: Physicochem. Eng. Asp. 680 (2024) 132675, https://doi.org/10.1016/j.colsurfa.2023.132675.
[8] L. Weiwei, Y. Xin, S. Keqiang, Z. Baohua, G. Guang, Unraveling the sources and fluorescence compositions of dissolved and particulate organic matter (DOM and POM) in Lake Taihu, China, Environ. Sci. Pollut. Res. 26 (2019) 4027–4040, https://doi.org/10.1007/s11356-018-3873-2.
[9] B. Wang, Y. Ma, S. Wang, L. Zhang, J. Liang, H. Li, L. Wu, L. Bi, Preparation of hybrid films containing polyoxometalate and fluorescein and their electrochemically induced fluorescence switching behaviors, J. Mater. Chem. C 2 (2014) 4423–4427, https://doi.org/10.1039/C3TC32306D.
[10] K.I. Aly, M.M. Sayed, M.G. Mohamed, S.W. Kuo, O. Younis, A facile synthetic route and dual function of network luminescent porous polyester and copolyester

containing porphyrin moiety for metal ions sensor and dyes adsorption, Micropor. Mesopor. Mater. 296 (2020) 110063, https://doi.org/10.1016/j.micromeso.2020.110063.
[11] M. Madhu, S. Santhoshkumar, C.W. Hsiao, W.L. Tseng, S.W. Kuo, M.G. Mohamed, Selective and sensitive detection of Fe^{3+} ions using a red-emissive fluorescent probe based on triphenylamine and perylene-linked conjugated microporous polymer, Macromol. Rapid Commun. 45 (2024) 2400263, https://doi.org/10.1002/marc.202400263.
[12] B. Qin, H. Chen, H. Liang, L. Fu, X. Liu, X. Qiu, S. Liu, R. Song, Z. Tang, Reversible photoswitchable fluorescence in thin films of inorganic nanoparticle and polyoxometalate assemblies, J. Am. Chem. Soc. 132 (2010) 2886–2888, https://doi.org/10.1021/ja908201x.
[13] M.G. Mohamed, N.Y. Liu, A.F.M. EL-Mahdy, S.W. Kuo, Ultrastable luminescent hybrid microporous polymers based on polyhedral oligomeric silsesquioxane for CO_2 uptake and metal ion sensing, Micropor. Mesopor. Mater. 311 (2021) 110695, https://doi.org/10.1016/j.micromeso.2020.110695.
[14] K. Zheng, P. Ma, Recent advances in lanthanide-based POMs for photoluminescent applications, Dalton Trans 53 (2024) 3949–3958, https://doi.org/10.1039/D3DT03999D.
[15] X. Zhang, Y. Zhang, J. Ying, B. Zhang, C. Wang, A. Tian, A series of POM-based compounds constructed by piperazine and morpholine derivatives: characterization, selective photocatalytic and electrochemical/fluorescence sensing properties, J. Solid State Chem. 295 (2021) 121888, https://doi.org/10.1016/j.jssc.2020.121888.
[16] G. Geisberger, E.B. Gyenge, D. Hinger, P. Bösiger, C. Maake, G.R. Patzke, Synthesis, characterization and bioimaging of fluorescent labeled polyoxometalates, Dalton Trans. 42 (2013) 9914–9920, https://doi.org/10.1039/C3DT50414J.
[17] A. Parrot, A. Bernard, A. Jacquart, S.A. Serapian, C. Bo, E. Derat, O. Oms, A. Dolbecq, A. Proust, R. Métivier, P. Mialane, G. Izzet, Photochromism and dual-color fluorescence in a polyoxometalate–benzospiropyran molecular switch, Angew Chem. Int. Ed. 129 (2017) 4950–4954, https://doi.org/10.1002/anie.201701860.
[18] Q. Shen, G. Song, H. Lin, H. Bai, Y. Huang, F. Lv, S. Wang, Sensing, imaging, and therapeutic strategies endowing by conjugate polymers for precision medicine, Adv. Mater. 36 (2024) 2310032, https://doi.org/10.1002/adma.202310032.
[19] M.G. Mohamed, M.H. Elsayed, C.J. Li, A.E. Hassan, I.M.A. Mekhemer, A.F. Musa, M.K. Hussien, L.C. Chen, K.H. Chen, H.H. Chou, S.W. Kuo, Reticular design and alkyne bridge engineering in donor–π–acceptor type conjugated microporous polymers for boosting photocatalytic hydrogen evolution, J. Mater. Chem. A 12 (2024) 7693–7710, https://doi.org/10.1039/D3TA07309B.
[20] B. Prusti, S. Tripathi, P.K. Samanta, M. Chakravarty, Vinylene-linked conjugated microporous polymer decorated with electron-rich units: a single-component white light emitting device, Adv. Opt. Mater. 12 (2024) 2301746, https://doi.org/10.1002/adom.202301746.
[21] M.H. Lin, M.G. Mohamed, C.J. Lin, Y.J. Sheng, S.W. Kuo, C.L. Liu, Achieving high zT with carbon nanotube/conjugated microporous polymer thermoelectric nanohybrids by meticulous molecular geometry design, Adv. Funct. Mater. 34 (2024) 2406165, https://doi.org/10.1002/adfm.202406165.
[22] P. Hajivand, J.C. Jansen, E. Pardo, D. Armentano, T.F. Mastropietro, A. Azadmehr, Application of metal-organic frameworks for sensing of VOCs and other volatile biomarkers, Coord. Chem. Rev. 501 (2024) 215558, https://doi.org/10.1016/j.ccr.2023.215558.
[23] M.G. Mohamed, B.X. Su, S.W. Kuo, Robust nitrogen-doped microporous carbon via crown ether-functionalized benzoxazine-linked porous organic polymers for enhanced CO_2 adsorption and supercapacitor applications, ACS Appl. Mater. Interfaces 16 (2024) 40858–40872, https://doi.org/10.1021/acsami.4c05645.
[24] S.M. Mousavi, F.F. Nezhad, M.H. Akmal, R.H. Althomal, N. Sharma, V. Rahmanian, R. Azhdari, A. Gholami, M.M. Rahman, W.H. Chiang, Recent advances and synergistic effect of bioactive zeolite imidazolate frameworks (ZIFs) for biosensing applications, Talanta 275 (2024) 126097, https://doi.org/10.1016/j.talanta.2024.126097.
[25] M. Ejaz, M.G. Mohamed, Y.T. Chen, K. Zhang, S.W. Kuo, Porous carbon materials augmented with heteroatoms derived from hyperbranched biobased benzoxazine resins for enhanced CO_2 adsorption and exceptional supercapacitor performance, J. Energy Storage 78 (2024) 110166, https://doi.org/10.1016/j.est.2023.110166.
[26] Q. Wang, M. Unno, H. Liu, Dual-Function near-infrared emitting aerogel-based device for detection and sunlight-driven photodegradation of antibiotics: realizing the processability of silsesquioxane-based fluorescent porous materials, Adv. Funct. Mater. 33 (2023) 2214875, https://doi.org/10.1002/adfm.202214875.
[27] S. Settele, C.A. Schrage, S. Jung, E. Michel, H. Li, B.S. Flavel, A. Stephen K. Hashmi, S. Kruss, J. Zaumseil, Ratiometric fluorescent sensing of pyrophosphate with sp^3-functionalized single-walled carbon nanotubes, Nat. Commun. 15 (2024) 706, https://doi.org/10.1038/s41467-024-45052-1.
[28] X. Guan, H. Li, L. Chen, G. Qi, Y. Jin, Glass capillary-based nanopores for single molecule/single cell detection, ACS Sens. 8 (2023) 427–442, https://doi.org/10.1021/acssensors.2c02102.
[29] Y.Y. Pan, W.M. Yin, R.J. Meng, Y.R. Guo, J.G. Zhang, Q.J. Pan, Productive preparation of N-doped carbon dots from sodium lignosulfonate/melamine formaldehyde foam and its fluorescence detection of trivalent iron ions, RSC adv. 11 (2021) 24038–24043, https://doi.org/10.1039/D1RA03279H.
[30] S.V. Chaganti, S.U. Sharma, M. Ibrahim, A. Basit, P.N. Singh, S.W. Kuo, M. G. Mohamed, Redox-active a pyrene-4,5,9,10-tetraone and thienyltriazine-based conjugated microporous polymers for boosting faradaic supercapacitor energy storage, J. Power Sources 627 (2025) 235848, https://doi.org/10.1016/j.jpowsour.2024.235848.
[31] R. Gao, W. Zhao, Q. Qiu, A. Xie, S. Cheng, Y. Jiao, X. Pan, W. Dong, Fluorescent conjugated microporous polymer (CMP) derived sensor array for multiple Organic/Inorganic contaminants detection, Sens. Actuators B: Chem. 320 (2020) 128448, https://doi.org/10.1016/j.snb.2020.128448.
[32] X. Liu, Y. Xu, D. Jiang, Conjugated microporous polymers as molecular sensing devices: microporous architecture enables rapid response and enhances sensitivity in fluorescence-on and fluorescence-off sensing, J. Am. Chem. Soc. 134 (2012) 8738–8741, https://doi.org/10.1021/ja303448r.
[33] A. Basit, Y.C. Kao, Y.A. El-Ossaily, S.W. Kuo, M.G. Mohamed, Rational engineering and synthesis of pyrene and thiazolo [5,4-d] thiazole-functionalized conjugated microporous polymers for efficient supercapacitor energy storage, J. Mater. Chem. A 12 (2024) 30508–30521, https://doi.org/10.1039/D4TA05908E.
[34] M.G. Mohamed, M.H. Elsayed, A.E. Hassan, A. Basit, I.M.A. Mekhemer, H.H. Chou, K.H. Chen, S.W. Kuo, Hybrid porous polymers combination of octavinylsilsesquioxane/pyrene with benzothiadiazole units for robust energy storage and efficient photocatalytic hydrogen production from water, ACS Appl. Polym. Mater. 6 (2024) 5945–5956, https://doi.org/10.1021/acsapm.4c00655.
[35] M. Ejaz, M.G. Mohamed, W.C. Huang, S.W. Kuo, Pyrene-based covalent organic polymers with nano carbonaceous composites for efficient supercapacitive energy storage, J. Mater. Chem. A 11 (2023) 22868–22883, https://doi.org/10.1039/D3TA02741D.
[36] D. Chen, C. Liu, J. Tang, L. Luo, G. Yu, Fluorescent porous organic polymers, Polym. Chem. 10 (2019) 1168–1181, https://doi.org/10.1039/C8PY01620H.
[37] C. Wang, S. Ma, L. Pan, W. Wu, Y. Wei, J. Ou, Cyclized conjugated microporous polymer-coated silica nanospheres as fluorescent sensors for iron (III) and chromium (III), Chem. Eng. J. 435 (2022) 134368, https://doi.org/10.1016/j.cej.2021.134368.
[38] M.G.M. Bai, H.V. Babu, V. Lakshmi, M.R. Rao, Structure–property–function relationship of fluorescent conjugated microporous polymers, Mater. Chem. Front. 5 (2021) 2506–2551, https://doi.org/10.1039/D0QM00769B.
[39] X. Li, Z. Li, Y.W. Yang, Tetraphenylethylene-interweaving conjugated macrocycle polymer materials as two-photon fluorescence sensors for metal ions and organic molecules, Adv. Mater. 30 (2018) 1800177, https://doi.org/10.1002/adma.201800177.
[40] M.G. Mohamed, H.Y. Hu, M. Madhu, M. Ejaz, S.U. Sharma, W.L. Tseng, M. M. Samy, C.W. Huang, J.T. Lee, S.W. Kuo, Construction of ultrastable conjugated microporous polymers containing thiophene and fluorene for metal ion sensing and energy storage, Micromachines 13 (2022) 1466, https://doi.org/10.3390/mi13091466.
[41] W.B. Tseng, M.J. Wu, C.Y. Lu, A.S.K. Kumar, W.L. Tseng, Aptamer-based flares hybridized with single-stranded DNA-conjugated MoS_2 nanosheets for ratiometric fluorescence sensing and imaging of potassium ions and adenosine triphosphate in human fluids and living cells, Spectrochim. Acta Mol. Biomol. Spectrosc. 309 (2024) 23781, https://doi.org/10.1016/j.saa.2023.123781.
[42] M.G. Mohamed, H.Y. Hu, M. Madhu, M.M. Samy, I.M.A. Mekhemer, W.L. Tseng, H. H. Chou, S.W. Kuo, Ultrastable two-dimensional fluorescent conjugated microporous polymers containing pyrene and fluorene units for metal ion sensing and energy storage, Eur. Polym. J. 189 (2023) 11980, https://doi.org/10.1016/j.eurpolymj.2023.111980.
[43] M. Madhu, S. Santhoshkumar, W.B. Tseng, A.S.K. Kumar, W.L. Tseng, Synthesis of rhenium disulfide nanodots exhibiting pH-dependent fluorescence and phosphorescence for anticounterfeiting and hazardous gas detection, Spectrochim. Acta Mol. Biomol. Spectrosc. 315 (2024) 124240, https://doi.org/10.1016/j.saa.2024.124240.
[44] S.G. Eswaran, T. Stalin, D. Thiruppathi, M. Madhu, S. Santhoshkumar, J. Warchol, A.S.K. Kumar, W.L. Tseng, N. Vasimalai, One-pot synthesis of carbon dots from neem resin and the selective detection of Fe(ii) ions and photocatalytic degradation of toxic dyes, RSC Sustain 2 (2024) 635–645, https://doi.org/10.1039/D3SU00404J.
[45] A. Basit, M.G. Mohamed, S.U. Sharma, S.W. Kuo, Thianthrene- and thianthrene tetraoxide-functionalized conjugated microporous polymers for efficient energy storage, ACS Appl. Polym. Mater. 6 (2024) 12247–12260, https://doi.org/10.1021/acsapm.4c02368.
[46] M.G. Mohamed, W.C. Chang, S.W. Kuo, Crown ether- and benzoxazine-linked porous organic polymers displaying enhanced metal ion and CO_2 capture through solid-state chemical transformation, Macromolecules 55 (2022) 7879–7892, https://doi.org/10.1021/acs.macromol.2c01216.
[47] M.G. Mohamed, T.C. Chen, S.W. Kuo, Solid-state chemical transformations to enhance gas capture in benzoxazine-linked conjugated microporous polymers, Macromolecules 54 (2021) 5866–5877, https://doi.org/10.1021/acs.macromol.1c00736.
[48] S.Y. Chang, A.M. Elewa, M.G. Mohamed, I.M.A. Mekhemer, M.M. Samy, K. Zhang, H.H. Chou, S.W. Kuo, Rational design and synthesis of bifunctional Dibenzo[g,p] chrysene-based conjugated microporous polymers for energy storage and visible light-driven photocatalytic hydrogen evolution, Mater. Today Chem. 33 (2023) 101680, https://doi.org/10.1016/j.mtchem.2023.101680.
[49] M. Zhang, R. Liu, F. Zhang, H. Zhao, X. Li, X. Lang, Z. Guo, Interfacial design of pyrene-based covalent organic framework for overall photocatalytic H_2O_2 synthesis in water, J. Colloid Interface Sci. 678 (2025) 1170–1180, https://doi.org/10.1016/j.jcis.2024.09.189.
[50] S.U. Sharma, M.H. Elsayed, I.M.A. Mekhemer, T.S. Meng, H.H. Chou, S.W. Kuo, M. G. Mohamed, Rational design of pyrene and thienyltriazine-based conjugated microporous polymers for high-performance energy storage and visible-light photocatalytic hydrogen evolution from water, Giant 17 (2024) 100217, https://doi.org/10.1016/j.giant.2023.100217.

[51] M. Rajasekar, P. Bhuvanesh, P. Varada, Recent trends in synthesis of photoluminescence based pyrene derivatives and their biomaterial applications. Results, Chem 6 (2023) 101008, https://doi.org/10.1016/j.rechem.2023.101008.
[52] Y. Takeo, J. Hirano, N. Fukui, H. Shinokubo, Effect of internal substituents on the properties of dibenzo[g,p]chrysene, Org. Lett. 25 (2023) 8484–8488, https://doi.org/10.1021/acs.orglett.3c03428.
[53] T. Xue, R. Guntermann, A. Biewald, D. Blätte, D.D. Medina, A. Hartschuh, T. Bein, Interpenetrated donor–acceptor heterojunctions in 2D conjugated dibenzo[g,p] chrysene-based kagome covalent organic frameworks, ACS Appl. Mater. Interfaces 16 (2024) 48085–48093, https://doi.org/10.1021/acsami.4c09286.
[54] W. Liu, Q. Liu, D. Wang, B.Z. Tang, Fluorescent porous materials based on aggregation-induced emission for biomedical applications, ACS Nano 18 (2024) 27206–27229, https://doi.org/10.1021/acsnano.4c08882.
[55] B. Bonillo, R.S. Sprick, A.I. Cooper, Tuning photophysical properties in conjugated microporous polymers by comonomer doping strategies, Chem. Mater. 28 (2016) 3469–3480, https://doi.org/10.1021/acs.chemmater.6b01195.
[56] J. Xiu, C. Li, G. Wang, Study on colorimetric sensing performance of covalent organic framework for highly selective and sensitive detection of Fe^{2+} and Fe^{3+} ions, J. Mol. Struct. 1276 (2023) 134779, https://doi.org/10.1016/j.molstruc.2022.134779.
[57] Z.S. Parr, C.B. Nielsen, Conjugated molecules for colourimetric and fluorimetric sensing of sodium and potassium, Mater. Chem. Front. 4 (2020) 2370–2377, https://doi.org/10.1039/D0QM00157K.
[58] K. Hirakawa, H. Segawa, Excitation energy transfer and photo-induced electron transfer in axial bispyrenyl phosphorus porphyrin derivatives: factors governing the competition between energy and electron transfer processes under the existence of intramolecular π–π interaction, J. Photochem. Photobiol., A 123 (1999) 67–76, https://doi.org/10.1016/S1010-6030(99)00043-X.
[59] B.C. Patra, S. Datta, S. Bhattacharya, A stimuli-responsive dual-emitting covalent organic framework shows selective sensing of highly corrosive acidic media via fluorescence turn-on signal with white light emission, ACS Appl. Mater. Interfaces 16 (2024) 7650–7659, https://doi.org/10.1021/acsami.3c15339.
[60] R. Bu, L. Zhang, X.Y. Liu, S.L. Yang, G. Li, E.Q. Gao, Synthesis and acid-responsive properties of a highly porous vinylene-linked covalent organic framework, ACS Appl. Mater. Interfaces 13 (2021) 26431–26440, https://doi.org/10.1021/acsami.1c01791.